

**Understanding the temperature induced aggregation of  
poly(*N*-isopropyl acrylamide)- and poly(*n*-propyl-2-oxazoline)-  
decorated silica nanoparticles**

Edward D.H. Mansfield,<sup>a,†</sup> Sergey K. Filippov,<sup>b,c</sup> Victor R. de la Rosa,<sup>d</sup> Michael T. Cook,<sup>e</sup>

Isabelle Grillo,<sup>f</sup> Richard Hoogenboom,<sup>d</sup> Adrian C. Williams,<sup>a</sup> Vitaliy V. Khutoryanskiy<sup>a\*</sup>

- a) School of Pharmacy, University of Reading, Whiteknights, Reading, RG6 6AD, Berkshire, United Kingdom, email: [v.khutoryanskiy@reading.ac.uk](mailto:v.khutoryanskiy@reading.ac.uk)
- b) Pharmaceutical Sciences Laboratory, Faculty of Science and Engineering, Åbo Akademi University, 20520 Turku, Finland
- c) Department of Chemistry and Chemical Technology, Al-Farabi Kazakh National University, 050040 Almaty, Kazakhstan
- d) Supramolecular Chemistry Group, Centre of Macromolecular Chemistry (CMaC), Department of Organic and Macromolecular Chemistry, Ghent University, Krijgslaan 281 S4, B-9000, Ghent, Belgium
- e) Research Centre in Topical Drug Delivery and Toxicology, Department of Pharmacy, Pharmacology and Postgraduate Medicine, University of Hertfordshire, Hatfield, Hertfordshire, UK, AL10 9AB
- f) Institut Laue-Langevin, 71 avenue des Martyrs, 38042 Grenoble, France

*KEYWORDS* Silica nanoparticles; Aggregation; SANS; temperature-responsive polymers; PNIPAM; poly(2-oxazoline)

---

Temperature-responsive nanomaterials have gained increasing interest over the past decade due their ability to undergo conformational changes *in situ*, in response to a change in temperature. One class of temperature-responsive polymers are those with lower critical solution temperature, which phase separate in aqueous solution above a critical temperature. When these temperature-responsive polymers are grafted to a solid nanoparticle, a change in their surface properties occurs above this critical temperature, from hydrophilic to more hydrophobic, giving them a propensity to aggregate. This study explores the temperature induced aggregation of silica nanoparticles functionalised with two temperature-responsive polymers with lower critical solution temperature (LCST) behavior, namely poly(*N*-isopropyl acrylamide) (PNIPAM), and poly(2-*n*-propyl-2-oxazoline) (PNPOZ) with similar molecular weights (5,000 Da) and grafting density. Using a combination of small-angle neutron scattering (SANS) and dynamic light scattering (DLS), we probed subtle differences in the aggregation processes for PNIPAM- and PNPOZ-

decorated silica nanoparticles. The nanoparticles decorated with PNIPAM and PNPOZ show similar aggregation behavior that was independent of polymer structure, whereby aggregation starts by the formation of small aggregates. A further increase in temperature leads to interaction between these aggregates and results in full-scale aggregation and subsequent phase separation.

---

## 1.0 Introduction

“Smart” nanomaterials are gaining interest in both academia and industry, due to their ability to undergo reversible changes in response to an external stimulus, such as changes in temperature or pH.<sup>1</sup> In particular, temperature-responsive polymers (TRPs) can change their physicochemical properties depending on temperature.<sup>2</sup> One class of TRPs are those with lower critical solution temperature (LCST), which phase separate above a critical temperature. At temperatures below the LCST, the polymer in diluted solution is hydrophilic in nature, taking an expanded coil conformation, and above the LCST it becomes more hydrophobic due to entropic dehydration leading to collapse into a globule followed by macroscopic phase separation of the high polymer concentration phase. Alternatively, the polymer can initially form clusters upon initial dehydration, which subsequently undergo a phase separation transition upon further dehydration. The aggregation pathway depends on the polymer molecular weight, concentration, and structure.<sup>3-4</sup> By tethering TRPs to a nanoparticle surface, the LCST of a polymer can change, in part due to steric hindrance caused by the dense polymer packing on the surface leading to enhanced polymer-polymer interactions that compete for hydration,<sup>5</sup> suggesting that the polymers will behave differently when grafted to a solid core or when free in solution.

Herein, we examined the effect of temperature on the size and early stages of aggregation for silica nanoparticles decorated with PNIPAM and PNPOZ thermoresponsive polymers. PNIPAM is a widely studied TRP with an LCST of 32 °C.<sup>6</sup> Several molecular characteristics that govern PNIPAM phase transition, such as degree of polymerization (DP), dispersity, branching, chain end-groups, charges, and tacticity, have been identified and studied. It was reported that isotactic, meso-dyad rich, PNIPAM has a lower cloud point temperature than atactic PNIPAM.<sup>7-9</sup> Recent computer simulations confirmed that the number of meso dyad (m) groups in a polymer chain is a crucial parameter that has an impact on polymer solubility in general and cloud point temperature in particular.<sup>10-11</sup> For example, PNIPAM with a degree of polymerization (DP) of 56 and containing >80% meso-dyad groups is insoluble over the temperature range of 5-45 °C whereas a shorter PNIPAM polymer (DP=34) is completely insoluble in water at any temperature. Interestingly, the number of meso-dyads controls not only demixing temperature but also

dictates the aggregation pathway. A SANS study showed that PNIPAM coils with 46 % meso-dyads per unit chain show some contraction followed by sharp phase separation whereas polymers with 58% of meso-dyads shrink simultaneously with small cluster formation.<sup>12</sup>

Despite the large number of reports of PNIPAM-functionalized nanoparticles and moderate number of reports on poly(2-oxazoline)-functionalized nanoparticles, there is surprisingly little research into their early stages of aggregation. Given their wide applications in biomedical research, understanding the behavior of these polymers at different temperatures is essential, as it can drastically alter the bulk-properties of the materials.

There have been many reported applications for various PNIPAM functionalized nanoparticles, ranging from “smart-glass,”<sup>13</sup> photo-thermal therapy,<sup>14</sup> remote-controlled triggered drug release,<sup>15</sup> and bioimaging.<sup>16</sup> Poly(2-oxazolines) have gained increasing interest in recent years mainly due to their excellent biocompatibility, ease of synthesis, and functionalizable side-chains.<sup>17-18</sup> Additionally, some poly(2-oxazolines) exhibit LCST behaviour, which is highly dependent on the side chains. Poly(2-*n*-propyl-2-oxazoline), and poly(2-isopropyl-2-oxazoline) have reported LCST’s of 25 and 38 °C,<sup>19</sup> respectively, making them very interesting for controlled release studies. Thermoresponsive poly(2-oxazoline) coated nanoparticles have been reported as logic gates and for controlling aggregation and cellular uptake.<sup>20-23</sup>

Herein, we examine how the size and aggregation processes change as a function of temperature for PNIPAM- and PNPOZ-functionalized silica nanoparticles, where the isomeric PNIPAM and PNPOZ have similar molecular weight and grafting density, and determine the features of aggregation for these particles at different temperatures using Small Angle Neutron Scattering (SANS) (Fig 1).

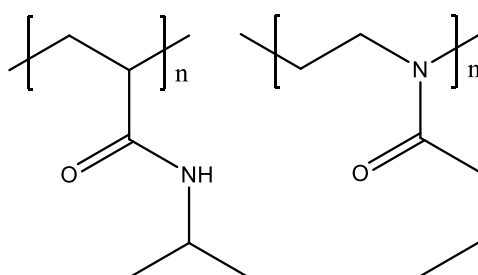


Fig 1. Structure of PNIPAM and PNPOZ repeat units.

## 2.0 Materials and methods

### 2.1 Materials

(3-Mercaptopropyl)trimethoxysilane (MPTS) (95 % purity), maleimide-terminated PNIPAM (average molecular weight 5 kDa), methanol and ethanol were purchased from Sigma-Aldrich (Gillingham, UK). Acetonitrile was obtained from Acros (UK). Dimethyl sulfoxide (DMSO) was obtained from Fisher Scientific (UK), and D<sub>2</sub>O from VWR International (UK). All other chemicals and reagents (including solvents) were of analytical grade or higher and were purchased from Sigma-Aldrich unless otherwise stated. All water used in this study was ultrapure water generated from a PureLab UHQ water purification system (18 MΩ), unless otherwise stated. Propargyl benzenesulphonate was distilled prior to use. 2-*n*-Propyl-2-oxazoline was synthesised as previously reported<sup>24</sup> and was distilled over barium oxide before use. Acetonitrile was dried over molecular sieves (3Å), and tetramethylammonium hydroxide in methanol (25 wt.%) was used as received.

### 2.2 Synthesis of thiolated silica nanoparticles

Thiolated silica nanoparticles were synthesized by the self-condensation of MPTS according to previously published methods, with no further modification.<sup>25-26</sup> 0.75 mL MPTS was added to 20 mL DMSO, followed by 0.5 mL of 0.5 mol/L aqueous NaOH. The reaction mixture was left stirring at room temperature for 24 h, whilst being continuously bubbled through with air. The formation of nanoparticles was observed by the appearance of a white turbid solution.

The obtained nanoparticles were purified by dialysis using a cellulose membrane with a molecular-weight cut-off of 12-14 kDa (Medicell International Ltd, UK). The particles were sealed inside the tubing and dialyzed against 4 L deionized water, over a 48 h period. A minimum of eight water changes were carried out. Following dialysis, three 1 mL aliquots were removed and frozen for lyophilization. The remainder was stored at 4 °C until further use.

### 2.3 Poly(2-*n*-propyl-2-oxazoline) (PNPOZ) synthesis and characterization

All reagents were stored and handled under dried nitrogen atmosphere in a glovebox (Vigor gas purification technologies, Inc.). Polymer synthesis was performed as previously reported.<sup>27,28</sup> A 4 M solution of the 2-*n*-propyl-2-oxazoline monomer was prepared in acetonitrile in the presence of 1/50 equivalents of propargyl benzenesulfonate. The polymerization mixture was heated to 100 °C in an aluminum heating

block for 60 min, cooled to 0 °C and the living polymer chains were terminated by addition of 1.1 equivalents of tetramethylammonium hydroxide under a dry nitrogen atmosphere. The polymerization mixture was kept stirring for 18 h at room temperature, after which the solvent was evaporated under reduced pressure. The polymer was re-dissolved in dichloromethane and precipitated in cold diethyl ether, yielding a white powder that was filtered and dried in a vacuum oven at 50 °C for 24 h. Polymer composition was confirmed by <sup>1</sup>H-NMR spectroscopy, MALDI-ToF MS (Matrix-Assisted Laser Desorption and Ionisation Time of Flight Mass Spectrometry) and size exclusion chromatography. Full characterization details of the obtained polymer can be found in the Supporting Information (Fig SI1-3).

<sup>1</sup>H-NMR spectra were recorded in CDCl<sub>3</sub> on a Bruker Avance 300 MHz spectrometer and processed using Bruker software (TOPSPIN 3.0). Size exclusion chromatography (SEC) was performed on an Agilent 1260-series equipped with a 1260 ISO-pump, a 1260 Diode Array Detector, a 1260 Refractive Index Detector, using two Mixed-D 30 cm columns (Agilent) and a Mixed-D precolumn (Agilent) in series at 50 °C, with DMA containing 50 mM of LiCl as eluent, at a flow rate of 0.593 mL/min. Molar masses and dispersity values were calculated against polymethylmethacrylate standards. MALDI-ToF MS used an Applied Biosystems Voyager-DE STR instrument equipped with a nitrogen laser operating at 337 nm, pulsed ion extraction source and reflectron detector. The laser pulse width was 3 ns at 3 Hz. Spectra were recorded in reflector mode with an acceleration voltage of 19 kV and delay of 400 ns. 100 single shot acquisitions were summed to give the spectra and the data were analyzed using Data Explorer software. Samples were prepared by dissolving the matrix 2-(4-hydroxyphenylazo)benzoic acid (HABA) in the solvent (acetone, 20 mg/mL), mixing with the polymer (1 mg/mL) and sodium iodide in acetone (15 mg/mL) that was used as a cationizing agent.

#### 2.4 Silica nanoparticle functionalization

For PNIPAM-functionalization, a 5 mL suspension of the thiolated silica nanoparticles (10 mg/mL) was diluted with 5 mL ultrapure water, followed by the addition of 100 mg maleimide-terminated PNIPAM. The reaction was left stirring for 24 h at room temperature and purified by dialysis as previously described for the thiolated silica nanoparticles.

For PNPOZ-functionalized particles, a 5 mL suspension of the thiolated nanoparticles (10 mg/mL), was diluted with 5 mL DMSO, and reacted with 100 mg of alkyne-terminated PNPOZ. The reaction was catalyzed by the addition of 200 µL triethylamine (TEA) and left for 96 h. Following completion, the sample was purified by dialysis as described for the thiolated silica nanoparticles. All particles were stored at 4 °C until further use.

## 2.5 Particle characterization

### 2.5.1 Size analysis

To characterize the particles, several complimentary techniques were used: Dynamic Light Scattering (DLS), Nanoparticle Tracking Analysis (NTA) and TEM were used to determine particle size, followed by FT-IR and FT-Raman spectroscopy, thermogravimetric analysis (TGA) and Ellman's assay for determination of surface functionality.

DLS measurements were recorded using a Zetasizer NanoZS (Malvern Instruments Ltd., UK). Each nanoparticle suspension was diluted ten-fold using ultrapure water before adding to low-volume cuvettes (Fisher Scientific, UK) and placement in the DLS instrument. A temperature ramp study was then undertaken between 20 and 50 °C. Measurements were taken every 1 °C, with 10 min equilibration before each measurement to ensure thermal equilibration. All readings were for an average of 12 runs, at 10 seconds per run. This was repeated three times for each measurement. Three independent samples were measured for each particle type. In all cases, a refractive index of 1.432 was used, based on the work of van der Pol *et al.*<sup>29</sup> The results are presented as the mean  $\pm$  standard deviation of the determined z-average values for three independent repeats. In addition to particle size measurements, the Zetasizer NanoZS was also used to determine the  $\xi$ -potential of the nanoparticle suspensions over the same temperature range. Again, a ten-fold dilution was used from stock, and the samples placed in DTS-1070 folded capillary tubes, which were sealed to prevent solvent evaporation. Each measurement was carried out in triplicate over an average of 20 runs, which was repeated for three independent samples. The results were processed using the Smoluchowski model ( $F_{ka} = 1.50$ ) and are presented as the mean  $\pm$  standard deviation of three independent repeats.

NTA measurements used an LM10 system with LM14 laser module and top plate, and green 532 nm laser (Malvern Instruments, UK). NTA requires very low concentrations of nanoparticles in suspension, as each nanoparticle is individually tracked. Therefore, samples were diluted 1:10,000 from the stock solution. Samples were then placed in a 1 mL syringe in a syringe pump set to a flow rate of 30 AU. As NTA works by tracking individual particles, having the system under flow allows a larger number of particles to be measured, and better represents the sample. Videos were recorded for 60 s, 5 videos per individual sample, and 3 samples were measured in total. Analysis used the NTA v3.0 software that provides a diffusion coefficient value. Diffusion coefficients were further converted to hydrodynamic diameter by Stokes-Einstein equation using NTA software. All NTA sizing experiments were at room temperature (25 °C) under the constant syringe pump flow.

### 2.5.2 Surface functionality

FT-IR spectra were recorded using a Spectrum 100 FT-IR spectrometer (Perkin Elmer, UK). A small quantity of lyophilized nanoparticles was placed on the sample holder and spectra were recorded from an average of 32 scans, at a resolution of  $4\text{ cm}^{-1}$ . Prior to analysis, a background spectrum was recorded and subtracted from the sample spectra. Spectra were collected between  $4000$  and  $550\text{ cm}^{-1}$ .

FT-Raman experiments used a Nicolet NXR 9650 FT-Raman spectrometer (Thermo Scientific, UK). Prior to analysis, the instrument was calibrated against a sulfur standard. For sample analysis, lyophilized nanoparticles were placed in glass HPLC vials, about a quarter full and tapped to remove any air pockets. Spectra were recorded as the average from 1000 scans, between  $4000$  and  $10\text{ cm}^{-1}$ , at a resolution of  $4\text{ cm}^{-1}$ .

TGA experiments were performed on a Q500 instrument (TA Instruments, UK) using nitrogen as the inlet gas. Before analysis, the instrument was calibrated against an empty platinum TGA pan, loaded with an empty Tzero aluminium DSC pan. Lyophilized nanoparticles were then placed into the empty DSC pan, ensuring even coverage of the bottom of the pan. This was then placed into a platinum TGA pan and loaded into the instrument. Thermal decomposition was measured by a temperature ramp between  $35$  and  $500\text{ }^{\circ}\text{C}$  at  $10\text{ }^{\circ}\text{C}/\text{min}$ . Polymer loading was determined by subtracting the weight loss observed for unfunctionalized silica nanoparticles from the weight loss seen for the functionalized silica nanoparticles. This was then expressed as a percentage of total mass.

Transmission Electron Microscope (TEM) images were recorded on a Phillips CM20 analytical TEM using a 4 megapixel AMT camera. An accelerating voltage of  $200\text{ kV}$  was used. Samples were prepared by placing a drop of nanoparticle suspension in aqueous dispersion onto a section of parafilm. A Holey Carbon film 300 mesh copper grid (HC300Cu, EMResolutions, UK) was then placed onto the drop and left for 1 minute. The grid was left to air dry before being placed in the instrument, and images recorded.

Ellman's assay was used to quantify the amount of reactive thiol groups present on nanoparticle surfaces. The procedure utilized was that of Bravo-Osuna et al with minor modifications.<sup>30</sup>  $3\text{ mg}$  of dry particles were re-suspended in  $10\text{ mL}$  phosphate buffer ( $\text{pH } 8$ ,  $0.5\text{ mol/L}$ ), and allowed to incubate for 1 hour. Ten aliquots ( $0.5\text{ mL}$ ) were individually placed in Eppendorf vials and reacted with  $0.5\text{ mL}$  5,5'-dithiobis-(2-nitrobenzoic acid) ( $0.3\text{ mg/mL}$ ) for 2 hours in the dark.  $200\text{ }\mu\text{L}$  aliquots were then pipetted into a 96 well plate (three repeats for each Eppendorf vial), and the absorbance measured at  $420\text{ nm}$  using a BioTek Epoch plate reader. L-cysteine-HCl solutions were used as standards in the concentration range of  $3.125\text{ }\mu\text{M}$  to  $12.69\text{ }\mu\text{M}$ , and reacted under the same conditions as for the nanoparticles.

## 2.6 Small Angle Neutron Scattering

Small angle neutron scattering (SANS) is a powerful technique to probe structural changes occurring in a system in response to an external stimulus, such as temperature, and relating this information to any higher-order structures existing. Here, SANS experiments were used to investigate structural changes in the polymer-decorated nanoparticles at different temperatures, and to determine the structure formed by interacting particles. Experiments were performed on the D11 instrument at the Institute Laue–Langevin, Grenoble (DOI: 10.5291/ILL-DATA.9-12-422). An incident wavelength of 8 Å coupled with detector distances of 1.2 m, 8 m and 28 m were used to cover a  $q$ -range of  $2 \times 10^{-3}$  to  $0.3 \text{ \AA}^{-1}$ , where  $q$  is defined as:

$$q = \frac{4\pi \sin \frac{\theta}{2}}{\lambda}$$

Here,  $\theta$  is the scattering angle, and  $\lambda$  is the wavelength of the incidence neutron beam. Data were recorded on a 2D  $^3\text{He}$  detector and, in all cases, were radial averaged and corrected for transmission, detector efficiency and a background of pure  $\text{D}_2\text{O}$ . The resulting data were converted into a scattering cross-section ( $\partial\Sigma/\partial\Omega$  vs  $q$ ), and placed on an absolute scale ( $I(q)$ ). Prior to any analysis, the incoherent background was subtracted.

Given that deuterium provides a greater contrast to neutrons during SANS experiments compared to hydrogen, prior to the experiment, samples were dialyzed against  $\text{D}_2\text{O}$  using a 7 kDa molecular-weight cut-off membrane (Medicell International, UK). A 1 mL aqueous suspension of particles was added into the membrane and sealed, before placing into a vial containing  $\sim 30$  mL  $\text{D}_2\text{O}$ .  $\text{D}_2\text{O}$  was replaced every 6 hours for a total of 3 changes. Following dialysis, samples were placed in glass vials and sealed with parafilm. Samples were then placed in 1 mm Hellma cuvettes, sealed with a PTFE stopper, and placed in the beam-line. Scattering cross-sections were obtained for PNIPAM and PNPOZ-silica nanoparticles at 25, 30, 34, and 40 °C, where the temperature was controlled by an external water circulation system. No sample filtration was used for SANS experiments.

Data fitting used the SASfit program,<sup>31</sup> using DLS and TEM data to provide the parameters. Various form factors were used depending on the sample and temperature and are described below. Due to the low concentrations of nanoparticles in solution we neglect interparticle interactions.

### 2.6.1 Spherical shell model:

The spherical shell form factor has the following form,

$$I(q) = \left[ 4\pi(R_{core} + \Delta R_{shell})^3 (\Delta SLD_{shell}) \cdot \frac{\sin(q(R_{core} + \Delta R_{shell})) - (R_{core} + \Delta R_{shell})q \cos(q(R_{core} + \Delta R_{shell}))}{(q(R_{core} + \Delta R_{shell}))^3} - 4\pi R_{core}^3 (\Delta SLD_{core}) \cdot \frac{\sin(qR_{core}) - R_{core}q \cos(qR_{core})}{(qR_{core})^3} \right]^2 \quad (1)$$

Where  $R_{core}$  is the core radius,  $\Delta R_{shell}$  is the thickness of the shell,  $\Delta SLD_{shell}$  is the difference in SLD (scattering length density) between the solvent and the shell,  $\Delta SLD_{core}$  is the difference in SLD between the solvent and the core. The  $\Delta SLD_{shell}$  and  $\Delta SLD_{core}$  were left as floating variables.

To account for nanoparticles polydispersity, a Schulz-Zimm distribution of  $R_{core}$  with polydispersity parameter  $\sigma$  was included in the following way,

$$SZ = \frac{R_{core}^Z}{\Gamma(Z+1) \langle R_{core} \rangle^{Z+1}} \exp \left[ -\frac{(Z+1)R_{core}}{\langle R_{core} \rangle} \right] \quad (2)$$

where  $Z = \frac{1}{\sigma^2} - 1$

### 2.6.2 Sphere with attached Gaussian chains Model

The scattered intensity curves were fitted using the model of a sphere with attached Gaussian chain having self-avoiding walk statistics implemented in SASFit software based on the model developed by Pedersen et al.<sup>32</sup>

The scattering curves in D<sub>2</sub>O could be fitted using the following function:

The overall scattering intensity of the sphere with attached Gaussian chain can be written as:

$$P_{sgc} = N_{agg}^2 \rho_{core}^2 P_{core}(q) + N_{agg} \rho_{chain}^2 P_{chain}(q) + 2N_{agg}^2 \rho_{core} \rho_{chain} S_{chain-core}(q) + N_{agg}(N_{agg} - 1) \rho_{chain}^2 S_{chain-chain}(q) \quad (3)$$

where  $N_{agg}^2 \rho_{core}^2 P_{core}(q)$  is the self-correlation term of the core;  $N_{agg} \rho_{chain}^2 P_{chain}(q)$  is the self-correlation term of the chains;  $2N_{agg}^2 \rho_{core} \rho_{chain} S_{chain-core}(q)$  is the cross-term between the core and chains and  $N_{agg}(N_{agg} - 1) \rho_{chain}^2 S_{chain-chain}(q)$  is the cross-term between different chains.  $N_{agg}$  is the aggregation number of polymer chains on the nanoparticle surface,  $\rho_{chain}$  and  $\rho_{core}$  are the excess scattering

lengths of a block in the corona and in the core, respectively.  $P_{core}(q)$  is the scattering of the spherical core:

$$P_{core}(q, R_{core}) = 3 \frac{(\sin(qR_{core}) - qR_{core}\cos(qR_{core}))}{(qR_{core})^3} \quad (4)$$

The scattering intensity for the brush is given by:

$$P_{chain}(q, r_{gchain}) = 2 \frac{\exp(-x) - 1 + x}{x^2} \quad (5)$$

where  $x = r_{gchain}^2 q^2$ ;  $r_{gchain}$  is the gyration radius of a polymer chain.

The contribution of the cross term between core and chains, which form the brush of wormlike micelles, is calculated using the equation:

$$S_{chain-core}(q, R_{core}, r_{gchain}, d) = \psi(qr_{gchain})P_{core}(q, R_{core}) \frac{\sin(q[R_{core} + dr_{gchain}])}{q[R_{core} + dr_{gchain}]} \quad (6)$$

where  $\psi(qr_{gchain}) = \frac{1 - \exp(-x)}{x}$  is the form factor amplitude of the chain.

The contribution of the cross term between chains is calculated using the equation:

$$S_{chain-chain}(q, R_{core}, r_{gchain}, d) = \psi^2(qr_{gchain}) \left[ \frac{\sin(q[R_{core} + dr_{gchain}])}{q[R_{core} + dr_{gchain}]} \right]^2 \quad (7)$$

where  $d$  is parameter that accounts for non-penetration of the chains into the core.

The model has the following fitting parameters:  $R_{core}$  – core radius;  $r_{gchain}$  – gyration radius of polymer chains in the corona,  $N_{agg}$  is the aggregation number of polymer chains;  $\rho_{core}$  – excess scattering length of the spherical core;  $\rho$  – excess scattering length of a block unit in the corona.

Excess scattering lengths of the core and polymeric chains were known from literature data and from the polymer composition, and were chosen to be fixed during the fitting procedure. The  $R_{core}$  value was also fixed to 140 Å since this value was known from TEM and SANS fitting of unfunctionalized silica.

To account for nanoparticles polydispersity, a Schulz-Zimm distribution of  $R_{core}$  with polydispersity parameter  $\sigma$  was included (Eq. 2).

### 2.6.3 Mass Fractal Model

The mass-fractal model was used in addition to the sphere with attached Gaussian chains model to describe the upturn at low  $q$ :

$$I(q) = I_0 P_{MF}(q) \quad (8)$$

where,  $I_0$  is the forward scattering.  $P_{MF}(q)$  can be defined by:

$$P_{MF}(q) = \frac{\sin[(D-1)\arctan(q\xi)]}{(D-1)q\xi(1+q^2\xi^2)^{\frac{(D-1)}{2}}} \quad (9)$$

where  $\xi$  is the correlation length representing the cluster size,  $\xi^2 = \frac{2R_g^2}{D(D+1)}$  and  $D$  is the fractal dimension representing the self-similarity of the structure, and  $R_g$  is the gyration radius of a fractal cluster.

The model has the following fitting parameters:  $I_0$ ,  $D$ , and  $R_g$ .

### 3.0 Results and discussion

#### 3.1 Nanoparticle characterization

Following synthesis, all nanoparticles were characterized for size and surface functionality using DLS, NTA, and TEM. Initially, the hydrodynamic diameter was established by DLS and NTA immediately following functionalization and purification. Fig 1 shows the DLS size distributions and TEM images for the thiolated, PNIPAM-, and PNPOZ-functionalized silica nanoparticles; and Table 1 provides a summary of the physicochemical properties. NTA size distributions are presented in Supplementary Information, Fig SI4.

**Table 1. Physicochemical properties of polymer-functionalized and thiolated nanoparticles**

Nanoparticle	Z-		$\zeta$ - potential* (mV)	Mode diameter** (nm)	Grafting	
	Average diameter* (nm)	PDI*			density ( $\mu\text{g nm}^{-2}$ ) $\times 10^{-15}$	Free thiol ( $\mu\text{mol/g}$ )
<b>Thiolated silica</b>	52 $\pm$ 1	0.072	-46 $\pm$ 2	54 $\pm$ 1	-	212 $\pm$ 47
<b>PNIPAM- silica</b>	70 $\pm$ 1	0.111	-29 $\pm$ 1	63 $\pm$ 3	8.6	128 $\pm$ 10
<b>PNPOZ-silica</b>	61 $\pm$ 1	0.194	-21 $\pm$ 2	58 $\pm$ 1	9.8	14 $\pm$ 1

Values for columns annotated with \* were determined from DLS measurements. Those with \*\* were determined by NTA measurements. Grafting density was determined by TGA, and the free thiol content by Ellman's assay.

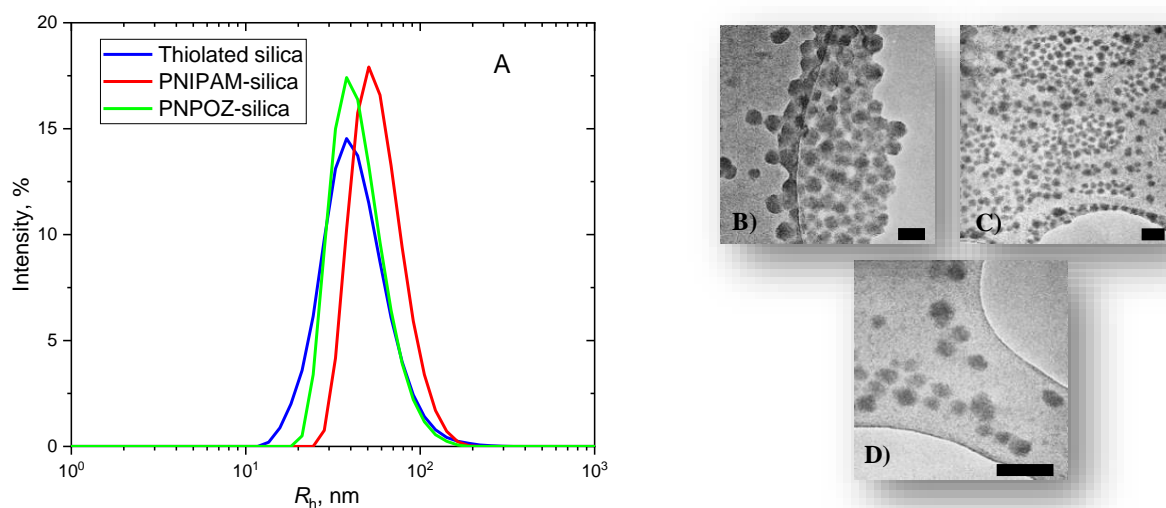


Fig 2. A) DLS size distributions for thiolated silica (blue), PNIPAM-silica (red) and PNPOZ-silica (green) nanoparticles measured at 25 °C. B, C, and D show TEM images for thiolated silica, PNIPAM-silica, and PNPOZ-silica, respectively. The scale-bars represent 50 nm for B, and 100 nm for C and D.

From Fig 2 and Table 1, it is clear that the size of the silica nanoparticles increases after polymer grafting, indicating successful functionalization of the particles. Both the z-average size (determined by DLS), and the modal particle diameter (determined by NTA) increase, along with an increase in polydispersity index (PDI) following polymer grafting. A reduction in both the  $\zeta$ -potential and the concentration of reactive thiol groups further confirm the presence of the polymer on the nanoparticle surface. It is proposed that a fraction of the thiol groups on the nanoparticles are in the form of thiolate anions, giving rise to the larger negative zeta-potential values of the thiolated nanoparticles.

The TGA analysis indicates the amount of polymer present on the particle surface, by subtracting the weight-loss on heating before and after functionalization. Values of  $8.6 \times 10^{-15}$  and  $9.8 \times 10^{-15}$   $\mu\text{g}\cdot\text{nm}^{-2}$  of polymer on the surface were obtained for PNIPAM and PNPOZ-silica, respectively, assuming a radius of 26 nm for plain silica particles constituting the core. These values were not significantly different from each other ( $p > 0.05$ ) and correspond to 1.0 and 1.2 chain per  $\text{nm}^2$ . Such grafting density values imply very close packing from which we expect a stretched conformation of the polymeric chains in the shell. TGA curves can be found in the Supplementary Information, Fig SI5.

In addition to size and polymer loading, FT-IR and FT-Raman were used to characterize the nanoparticles' surface functionality and confirmed the presence of polymer (Fig 3).

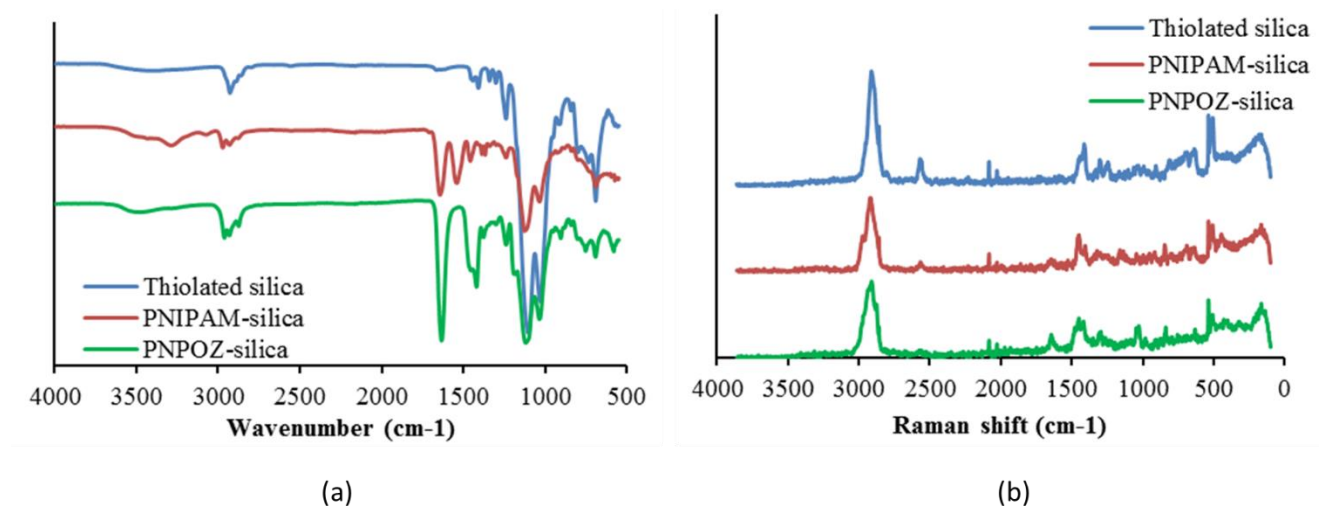


Fig 3 FT-IR (a) and Raman (b) spectra for thiolated silica (blue), PNIPAM-silica (red), and PNPOZ-silica (green) nanoparticles

The FT-IR spectrum of the thiolated silica particles (blue) shows two major peaks at  $1032$  and  $1102$   $\text{cm}^{-1}$  due to the Si-O-Si stretches from the disiloxane. The siloxane moiety of the nanoparticles exhibits two

distinct features between 1300 and 1000  $\text{cm}^{-1}$  due to the different functionalities attached to the silicon atoms (Si-O, and Si-C, respectively).<sup>33</sup> This agrees well with the nanoparticle structure proposed by Irmukhametova *et al.*<sup>25</sup> Both of these vibrational modes are evident in the spectra for functionalized particles (red and green), confirming the presence of the silica core in these samples. The FT-IR spectrum from PNIPAM functionalized silica nanoparticles has predominant peaks at 3298  $\text{cm}^{-1}$  (aliphatic C-H), 1632  $\text{cm}^{-1}$  (C=O), 1535  $\text{cm}^{-1}$  (N-H), and 1459  $\text{cm}^{-1}$  (aliphatic C-C). These features are not seen in the spectrum of the unfunctionalized silica and clearly demonstrate the presence of PNIPAM bound to the particle. Similarly, for the PNPOZ silica particles, the peaks at 2940  $\text{cm}^{-1}$  ( $\text{CH}_2$ ), 1630  $\text{cm}^{-1}$  (C=O), 1476  $\text{cm}^{-1}$  (C-H), 1422  $\text{cm}^{-1}$  ( $\text{CH}_3$ ), and 1236  $\text{cm}^{-1}$  (C-N) demonstrate the presence of PNPOZ in this sample.

The FT-Raman spectrum for thiolated silica (blue) shows principle peaks at 2880  $\text{cm}^{-1}$  (C-H), 2510  $\text{cm}^{-1}$  (S-H), 1400  $\text{cm}^{-1}$  ( $\text{CH}_2$ ), 1310  $\text{cm}^{-1}$  (C-C), 1250  $\text{cm}^{-1}$  (C-C), 631  $\text{cm}^{-1}$  (C-S), and  $\sim 500$   $\text{cm}^{-1}$  (Si-O-Si and S-S). Following PNIPAM functionalization, new peaks arise at 1628, and 837  $\text{cm}^{-1}$ , representing the C=O stretch and C-C vibrations in PNIPAM. PNPOZ has peaks at 1631  $\text{cm}^{-1}$  and 1024  $\text{cm}^{-1}$ , representing C=O and C-C vibrations, respectively. Functionalization of the nanoparticle surface also reduced the intensity of the thiol stretching mode at 2510  $\text{cm}^{-1}$ . From these data, it is evident that the thiolated silica nanoparticles were successfully functionalized with PNIPAM and PNPOZ.

### 3.2 Effect of temperature on particle aggregation

To study the effect of temperature on the particle size, PDI and  $\zeta$ -potential, DLS measurements were performed across a temperature ramp. The temperature range was chosen (20-50  $^{\circ}\text{C}$ ) to span across the reported LCST of both polymers (25 and 32  $^{\circ}\text{C}$  for PNPOZ and PNIPAM, respectively). The thiolated silica particles were also subjected to the same temperature ramp as a control to verify that the changes observed were due to the presence of the polymer and not a trait exhibited by the thiolated particles. Fig 5 illustrates the size and PDI dependence on temperature.

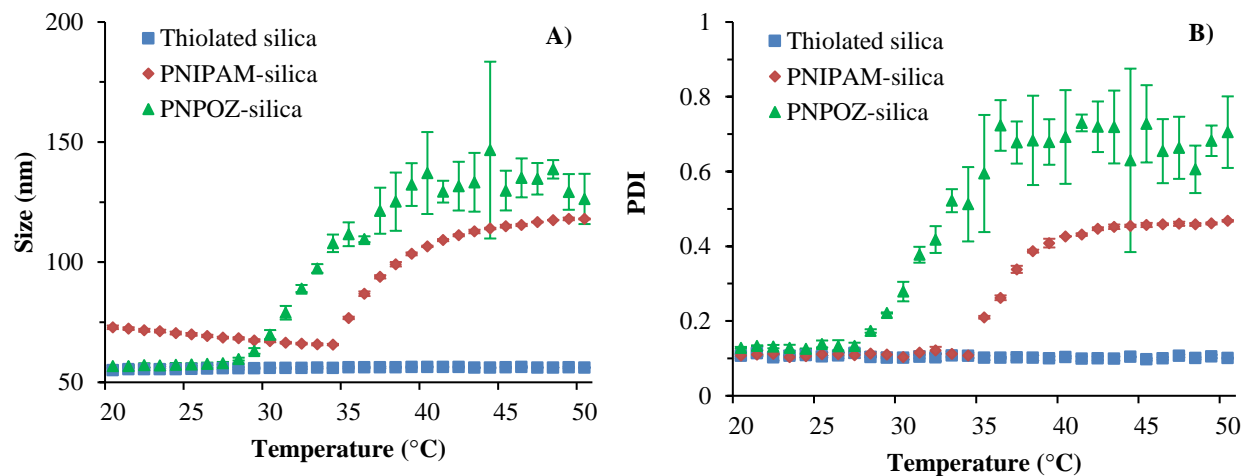


Fig 4. Size (A) and PDI (B) of thiolated silica, PNIPAM-silica, and PNPOZ-silica nanoparticles as a function of temperature. Results are the means of 3 repeats  $\pm$  standard deviation.

Fig 4A, shows that, as temperature increases, the particle size of the TRP-functionalized materials increases significantly ( $p < 0.05$ ) while it is invariant for the thiolated silica nanoparticles. The PNIPAM-silica nanoparticles show a steady increase in hydrodynamic diameter between 34 and 40 °C, after which it reaches a plateau. A similar trend is shown with the PDI values (Fig 4B) suggesting that the particles are forming aggregates as the temperature increases above 34 °C. Interestingly, the PDI values are remarkably consistent between the 3 independent repeats. These data for the onset of aggregation compare favorably with the known lower critical solution temperature for PNIPAM of 32 °C. A similar increase in size and PDI is seen for the PNPOZ-functionalized nanoparticles but with a lower onset temperature of 28-29 °C, again close to the LCST value of 25 °C. It is also evident from Fig 3 that the size and polydispersity recorded for the aggregating PNPOZ particles was more diverse than from the PNIPAM samples.

In addition to the size and PDI of the particles, their  $\zeta$ -potential was determined across the same temperature range (Fig 5). From these data, it is clear that there are changes in  $\xi$ -potential as temperature increases across all samples. The thiolated silica nanoparticles (Fig 5; blue) revealed a decrease in the negative  $\xi$ -potential as the temperature increases and there is a significant difference between the  $\xi$ -potential at 20 °C ( $-54 \pm 1$  mV) and that at 50 °C ( $-43 \pm 2$  mV) ( $p < 0.05$ ). Several authors reported the effect of temperature on the  $\xi$ -potential of various silicate particles.<sup>34-36</sup> The zeta potential of silica was found to be more negative with increasing temperature, which was related to the dissociation of the silanol groups at the interface.<sup>35</sup> The trend observed in our work for thiolated silica is clearly opposite, which is unex-

pected as pKa values generally tend to decrease with increasing temperature.<sup>37</sup> Therefore, it may be speculated that more thiols are engaged in disulfide bridges at elevated temperatures leading to an increase in zeta potential.

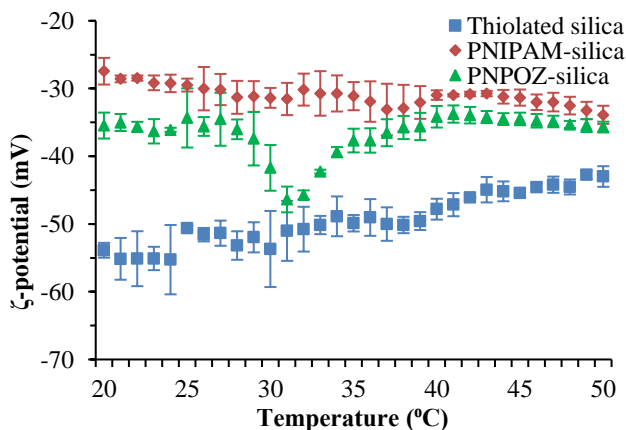


Fig 5.  $\zeta$ -potential of unfunctionalized thiolated silica, PNIPAM-silica, and PNPOZ-silica nanoparticles as a function of temperature. Results are the means of 3 repeats  $\pm$  standard deviation.

For the PNIPAM functionalized nanoparticles, although it may appear that there is a slight increase in  $\zeta$ -potential across the temperature range, the change is not statistically significant ( $p > 0.05$ ) and there is no inflection at temperatures where the particles aggregate. Similar effects of temperature on  $\zeta$ -potential of PNIPAM-functionalized colloids have been reported by other authors.<sup>38</sup>

The changes in  $\zeta$ -potential occurring for PNPOZ are rather unexpected. The  $\zeta$ -potential remains invariant until 27 °C, beyond which it becomes significantly ( $p < 0.05$ ) more negative up to 31 °C (from -31 to -46 mV), followed by a steady decrease in negativity between 32 and 40 °C (from -46 to -34 mV) and then remains essentially constant up to 50 °C. Although no significant difference can be observed between the initial  $\zeta$ -potential and the final  $\zeta$ -potential ( $p > 0.05$ ), there is a significant difference when the  $\zeta$ -potential drops to its lowest value; -46 mV ( $p < 0.05$ ). Considering this inflection alongside the size and PDI data (Fig 5B), this change occurs as the particles undergo the phase-transition, i.e. as the particles are aggregating. The point at which the  $\zeta$ -potential becomes more negative (27 °C) is the point at which the size and PDI also start to increase. Likewise, once the  $\zeta$ -potential has “recovered”, the particle size and PDI have plateaued. We do not have a clear understanding of these observations, albeit they hint at a difference in the phase transition mechanism for PNIPAM and PNPOZ.

The DLS data show that both PNIPAM and PNPOZ functionalized silica nanoparticles undergo temperature induced aggregation whereas no changes occur in the thiolated silica nanoparticles, confirming that it is the presence of the polymer causing these thermally-dependent events. To further investigate these findings, SANS experiments were employed.

### 3.3 Aggregation study

To further probe the mechanism of aggregation, SANS was employed to investigate the structural changes occurring at different temperatures, and to establish any interactions between particles. The scattered intensity in  $\text{cm}^{-1}$  of PNIPAM and PNPOZ-silica nanoparticles in  $\text{D}_2\text{O}$  measured at 4 different temperatures, chosen from the DLS profiles, are presented in Fig. 6. Due to the H-D isotopic effect, there is a certain mismatch between the thermoresponsive behavior in  $\text{H}_2\text{O}$  and  $\text{D}_2\text{O}$  for the same polymer. The cloud point temperature ( $T_{\text{cp}}$ , the temperature when the phase separation can be seen by simple observation (cloudiness) under heating) values for PNIPAM in  $\text{D}_2\text{O}$  are 3 °C higher in comparison with  $\text{H}_2\text{O}$  solution.<sup>39</sup> Thus, SANS data for PNIPAM coated silica nanoparticles in  $\text{D}_2\text{O}$  at 40 °C correspond to 37 °C in  $\text{H}_2\text{O}$ , i.e. just above  $T_{\text{cp}}$ , the same as PNPOZ-silica nanoparticles in  $\text{D}_2\text{O}$  at 34 °C.

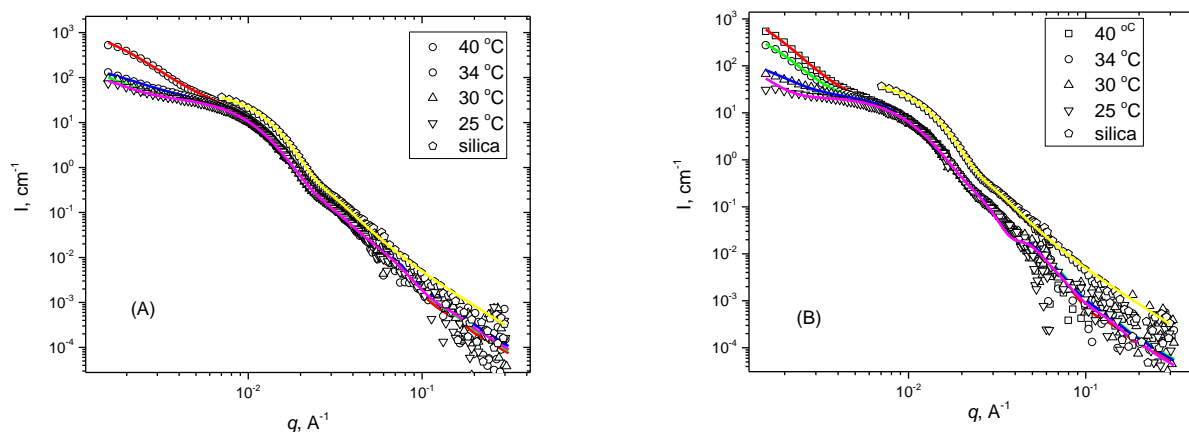


Fig 6. Scattering cross-section for PNIPAM- (A) and PNPOZ-silica (B) nanoparticles at different temperatures, as a function of  $q$ . Solid lines are fits. Note that the scattering profile for unmodified silica was not recorded at lower  $q$  because of the lack of beam time allocation.

The scattering profiles of the particles are almost superimposed for  $q$  values higher than  $0.01 \text{ \AA}^{-1}$ . An increase in intensity at low  $q$  is observed upon heating which occurs at 40°C for PNIPAM, whereas for

PNPOZ, it starts at 30°C and becomes more pronounced with increasing temperature. For both PNIPAM- and PNPOZ- decorated particles, the intensity of scattering changes at low  $q$  values upon heating ( $q < 0.004 \text{ \AA}^{-1}$ ). PNPOZ has lower demixing temperature than PNIPAM, and this is reflected in the scattering data. Particle scattering at high  $q$  values appears invariant with temperature, giving a strong evidence that the polymeric shell is nearly unaffected by increasing temperature over the range used here. However, at low  $q$  values the scattering intensity increases with temperature, suggesting higher order aggregation. For PNIPAM-silica nanoparticles (Fig 6A), the scattering cross-section appears curved at 40 °C at  $q < 0.004 \text{ \AA}^{-1}$ , suggesting aggregates of a specific size (as shown in DLS), whereas the same region in PNPOZ-silica nanoparticles appears linear.

To model these data, initially a spherical shell model with Schulz-Zimm polydispersity for the core radius was used for the unfunctionalized thiolated silica. The additional shell describes the thin layer of thiol groups on silica surface. For unfunctionalized thiolated particles, a diameter of 28.6 nm,  $\sigma$  of 0.29 for a core, and 0.5 nm for a shell was obtained, which corroborates literature values for previous work using SANS on these silica nanoparticles.<sup>40</sup> These values were used as a guide in modelling the PNIPAM and PNPOZ-silica nanoparticles. In comparison with the scattering of the unfunctionalized particles, larger aggregates form even below the  $T_{cp}$  for the functionalized materials. This can be seen by an increase in intensity rather than a turn-over in the scattering cross-section.

To determine the changes in nanoparticle structure exhibited by heating the samples, the scattering curves were fitted by a combination of form factors of a sphere with the attached Gaussian coils and mass-fractal. A summary of the fitting parameters and finding can be found in the Table 2 with exemplar fits in Fig 7.

**Table 2 Summary of the fitting data for PNIPAM- or PNPOZ-silica nanoparticles**

	T, °C	$R_{\text{core}}$ , Å	$\sigma$	$r_g$ , Å	$N_{\text{agg}}$	$D$	$R_g$ , Å	$I_0$ , $\text{cm}^{-1}$
Silica	25	143	0.29±0.04	5	-	-	-	
PNIPOZ	40	140	0.25±0.01	73.5±0.2	984±2	3.32±0.02	1847	3673
PNIPOZ	34	140	0.24±0.01	73.1±0.1	984±2	3.64±0.05	1520	1149
PNIPOZ	30	140	0.21±0.01	77.8±0.2	984±2	4.16±0.03	1351	185
PNIPOZ	25	140	0.17±0.01	84.4±0.2	984±2	4.69±0.03	1942	87
PNIPAM	40	140	0.27±0.01	66.7±0.1	1089±3	3.09±0.04	1343	1719
PNIPAM	34	140	0.27±0.01	67.8±0.1	1089±2	2.82±0.04	1333	239
PNIPAM	30	140	0.26±0.01	68.2±0.1	1089±1	3.77±0.05	1385	214
PNIPAM	25	140	0.28±0.01	68.5±0.2	1089±2	4.0±0.2	1366	159

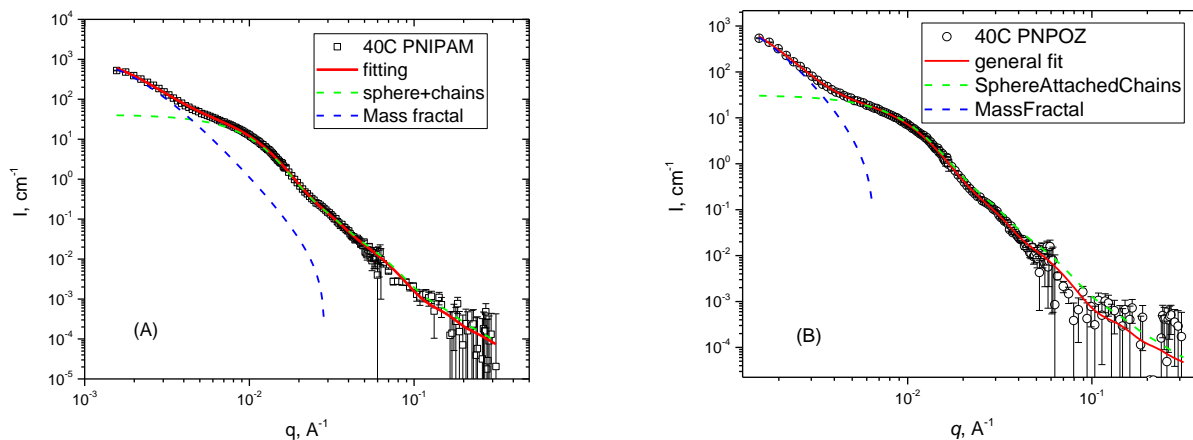


Fig 7. Scattering cross-section and individual contributions of form factors of a sphere with the attached Gaussian coils and mass-fractal for PNIPAM-silica (A) and PNPOZ-silica nanoparticles (B) at 40 °C.

From the PNIPAM and PNPOZ-decorated particle data, it is possible to conclude that at all temperatures, even below  $T_{\text{cp}}$ , the particles coexist with small fraction of aggregates as is represented by the upturn at low  $q$  values. Interestingly, there are only minor changes in the gyration radius ( $r_g$ ) value of a polymer chain attached to silica surface (Table 2); the shell becomes thinner with increases in temperature. The

most pronounced changes are observed for PNPOZ-decorated particles where  $r_g$  value changes from 84 to 73 Å, whereas PNIPAM-decorated particles have almost no temperature dependence of shell thickness, suggesting no significant collapse of the hydration polymeric shell. The aggregation numbers obtained from the fitting were 984 and 1089 for PNPOZ and PNIPAM decorated particles, respectively. As such, the grafting density of each polymer can be calculated as  $1.0 \times 10^{-15}$  and  $1.1 \times 10^{-15}$   $\mu\text{g}/\text{nm}^2$ , respectively, corresponding well to the TGA data (Table 1).

The forward scattering of mass fractal contribution,  $I_0$ , grows with elevating temperature suggesting that the number of clusters or their size, or both, increase with temperature. However, from these data, it is not possible to properly describe the shape and aggregations number of clusters since fitted  $R_g$  values are beyond the experimental  $q$  range and so are unreliable. However, we can conclude about the presence of aggregates and their growth below  $T_{cp}$  for both polymers.

The above results show that the two different temperature-responsive polymers studied have near identical early stage aggregation behaviour. From the SANS data, it is clear that the polymeric shell around the silica core remains essentially intact at different temperatures in the vicinity of  $T_{cp}$  as illustrated by the negligible decrease in the gyration radius of polymer chain mediated by the onset of aggregate formation. Given that there are just minor changes in the polymer shell, it is likely that the onset of aggregation starts before complete coil-to-globule collapse of the polymer shell. Similar behavior was observed for PNIPAM with high content of meso-dyads.<sup>12</sup> We hypothesize that the early stages of temperature-induced aggregation are governed by the partial dehydration of the polymeric chains, where some chains are more dehydrated than others. The local heterogeneities in partial dehydration can be induced by inhomogeneity in polymer grafting density, meso-dyad content or chain length. These metastable local hydrophobic patches function as bridges to form initial clusters that may further dehydrate during aggregation,<sup>41</sup> schematically depicted in Fig 7. Further dehydration leads to the formation of larger aggregates. This study is, to our knowledge, the first report on a critical comparison between these two temperature-responsive polymers grafted onto silica nanoparticles with regards to their mechanism of aggregation.

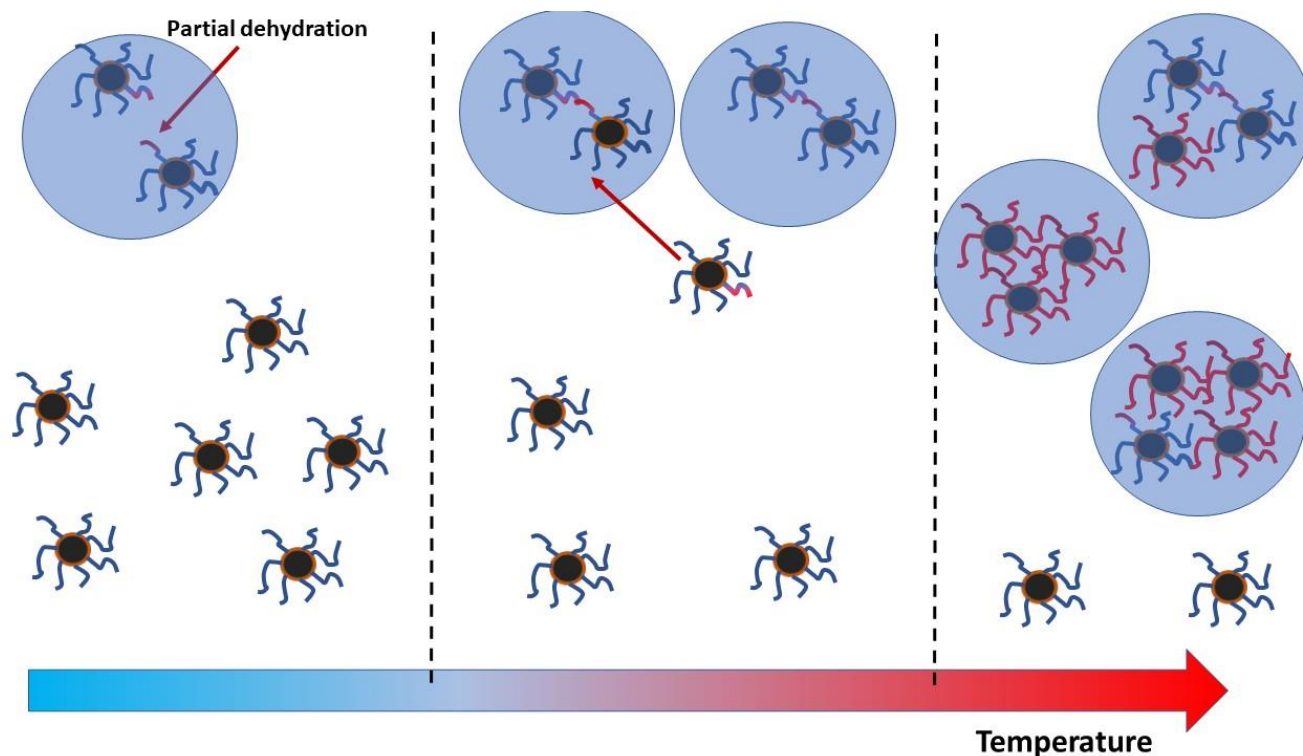


Fig 7. Proposed scheme of the aggregation of PNIPAM- and PNPOZ-silica nanoparticles with increasing temperature. At temperatures below  $T_{cp}$ , the vast majority of particles with a highly swollen shell coexist in solution with a negligible fraction of large aggregates. With temperature increasing, some polymeric chains in a shell undergo partial dehydration and such particles either join already formed aggregates making them bigger or start the nucleation of a new aggregate. Polymeric shell of the remaining particles stay in highly swollen state. Such process continues with more and more particles experiencing partial dehydration. This scenario describes the early stage of aggregation.

## 4.0 Conclusions

This work reports a detailed study on the mechanism of aggregation for two different temperature-responsive polymers (PNIPAM, and PNPOZ) grafted onto silica nanoparticles. Polymer grafting onto the particles was confirmed by molecular spectroscopy and quantified by thermogravimetric analysis, revealing successful conjugation and comparable grafting densities. Using a combination of small-angle neutron scattering (SANS) and dynamic light scattering (DLS), we have shown that there are subtle differences in the aggregation process for PNIPAM- and PNPOZ-decorated silica, which follow congruent mechanisms. For both polymers, aggregation begins with the formation of small clusters that interact with each other at higher temperatures and form larger aggregates resulting in phase separation. These clusters coexists with silica decorated with non-collapsed polymer chains. The observed picture resembles the behavior of PNIPAM chains with high content of meso-dyads suggesting that they are the key feature that controls the early stages of aggregation of polymer-functionalized nanoparticles. We believe that some local inhomogeneities in grafting density or meso-dyad content present in polymers are the driving force for the formation of clusters, which is responsible for the early-stages of aggregation. These findings reveal fundamental insight into this class of thermoresponsive nanotechnology to inform the development of novel advanced materials.

## Acknowledgements

The authors would like to thank Malvern Instruments and the University of Reading for funding the doctoral studies of EM. The Chemical Analysis Facility (University of Reading) is acknowledged for providing access to FT-IR/FT-Raman spectroscopy, TGA, and TEM. The Institute Laue-Langevin (proposal number 9-12-422, DOI: [10.5291/ILL-DATA.9-12-422](https://doi.org/10.5291/ILL-DATA.9-12-422)) is greatly thanked for allowing us access to D11 for neutron studies. V.R.R. would like to thank IWT (project 140800) for financial support. S.K.F. acknowledges the financial support of the grant BR05236446 from the Ministry of Science (Republic of Kazakhstan).

## AUTHOR INFORMATION

### Corresponding Author

\* School of Pharmacy, University of Reading, Whiteknights, Reading, Berkshire, UK, RG6 6AD

### Present Addresses

† STFC/UKRI, Polaris House, North Star Avenue, Swindon, SN2 1FL

## REFERENCES

1. Yoshida, M.; Lahann, J., Smart nanomaterials. *Acs Nano* **2008**, *2* (6), 1101-1107.
2. Khutoryanskiy, V. V.; Georgiou, T., *Temperature-responsive polymers: chemistry, properties and applications*. Wiley & sons: 2018.
3. Zhao, C.; Ma, Z.; Zhu, X. X., Rational design of thermoresponsive polymers in aqueous solutions: A thermodynamics map. *Progress in Polymer Science* **2019**, *90*, 269-291.
4. Zhang, Q.; Weber, C.; Schubert, U. S.; Hoogenboom, R., Thermoresponsive polymers with lower critical solution temperature: from fundamental aspects and measuring techniques to recommended turbidimetry conditions. *Materials Horizons* **2017**, *4* (2), 109-116.
5. Yu, Y.; Kieviet, B. D.; Liu, F.; Siretanu, I.; Kutnyanszky, E.; Vancso, G. J.; de Beer, S., Stretching of collapsed polymers causes an enhanced dissipative response of PNIPAM brushes near their LCST. *Soft Matter* **2015**, *11* (43), 8508-8516.
6. Halperin, A.; Kröger, M.; Winnik, F. M., Poly(N-isopropylacrylamide) Phase Diagrams: Fifty Years of Research. *Angewandte Chemie International Edition* **2015**, *54* (51), 15342-15367.
7. Ray, B.; Okamoto, Y.; Kamigaito, M.; Sawamoto, M.; Seno, K.; Kanaoka, S.; Aoshima, S., Effect of tacticity of poly(N-isopropylacrylamide) on the phase separation temperature of its aqueous solutions. *Polym J* **2005**, *37* (3), 234-237.
8. Ito, M.; Ishizone, T., Living anionic polymerization of N-methoxymethyl-N-isopropylacrylamide: Synthesis of well-defined poly (N-isopropylacrylamide) having various stereoregularity. *J Polym Sci Pol Chem* **2006**, *44* (16), 4832-4845.
9. Hirano, T.; Okumura, Y.; Kitajima, H.; Seno, M.; Sato, T., Dual roles of alkyl alcohols as syndiotactic-specificity inducers and accelerators in the radical polymerization of N-isopropylacrylamide and some properties of syndiotactic poly(N-isopropylacrylamide). *J Polym Sci Pol Chem* **2006**, *44* (15), 4450-4460.
10. Deshmukh, S. A.; Li, Z.; Kamath, G.; Suthar, K. J.; Sankaranarayanan, S. K. R. S.; Mancini, D. C., Atomistic insights into solvation dynamics and conformational transformation in thermo-sensitive and non-thermo-sensitive oligomers. *Polymer* **2013**, *54* (1), 210-222.
11. Deshmukh, S. A.; Sankaranarayanan, S. K. R. S.; Suthar, K.; Mancini, D. C., Role of Solvation Dynamics and Local Ordering of Water in Inducing Conformational Transitions in Poly(N-isopropylacrylamide) Oligomers through the LCST. *J Phys Chem B* **2012**, *116* (9), 2651-2663.
12. Nishi, K.; Hiroi, T.; Hashimoto, K.; Fujii, K.; Han, Y.-S.; Kim, T.-H.; Katsumoto, Y.; Shibayama, M., SANS and DLS Study of Tacticity Effects on Hydrophobicity and Phase Separation of Poly(N-isopropylacrylamide). *Macromolecules* **2013**, *46* (15), 6225-6232.
13. Zhu, M.-Q.; Wang, L.-Q.; Exarhos, G. J.; Li, A. D. Q., Thermosensitive Gold Nanoparticles. *Journal of the American Chemical Society* **2004**, *126* (9), 2656-2657.

14. Huang, X. H.; Jain, P. K.; El-Sayed, I. H.; El-Sayed, M. A., Plasmonic photothermal therapy (PPTT) using gold nanoparticles. *Laser Med Sci* **2008**, *23* (3), 217-228.
15. Baeza, A.; Guisasaola, E.; Ruiz-Hernández, E.; Vallet-Regí, M., Magnetically Triggered Multidrug Release by Hybrid Mesoporous Silica Nanoparticles. *Chemistry of Materials* **2012**, *24* (3), 517-524.
16. Yoon, T.-J.; Yu, K. N.; Kim, E.; Kim, J. S.; Kim, B. G.; Yun, S.-H.; Sohn, B.-H.; Cho, M.-H.; Lee, J.-K.; Park, S. B., Specific Targeting, Cell Sorting, and Bioimaging with Smart Magnetic Silica Core–Shell Nanomaterials. *Small* **2006**, *2* (2), 209-215.
17. Hoogenboom, R., Poly(2-oxazoline)s: A Polymer Class with Numerous Potential Applications. *Angewandte Chemie International Edition* **2009**, *48* (43), 7978-7994.
18. Sedlacek, O.; Monnery, B. D.; Filippov, S. K.; Hoogenboom, R.; Hruby, M., Poly(2-Oxazoline)s – Are They More Advantageous for Biomedical Applications Than Other Polymers? *Macromolecular Rapid Communications* **2012**, *33* (19), 1648-1662.
19. Hoogenboom, R.; Schlaad, H., Thermoresponsive poly(2-oxazoline)s, polypeptoids, and polypeptides. *Polymer Chemistry* **2017**, *8* (1), 24-40.
20. Koshkina, O.; Lang, T.; Thiermann, R.; Docter, D.; Stauber, R. H.; Secker, C.; Schlaad, H.; Weidner, S.; Mohr, B.; Maskos, M.; Bertin, A., Temperature-Triggered Protein Adsorption on Polymer-Coated Nanoparticles in Serum. *Langmuir* **2015**, *31* (32), 8873-8881.
21. Kurzhals, S.; Gal, N.; Zirbs, R.; Reimhult, E., Controlled aggregation and cell uptake of thermoresponsive polyoxazoline-grafted superparamagnetic iron oxide nanoparticles. *Nanoscale* **2017**, *9* (8), 2793-2805.
22. Morgese, G.; Causin, V.; Maggini, M.; Corrà, S.; Gross, S.; Benetti, E. M., Ultrastable Suspensions of Polyoxazoline-Functionalized ZnO Single Nanocrystals. *Chem Mater* **2015**, *27* (8), 2957-2964.
23. de la Rosa, V. R.; Zhang, Z.; De Geest, B. G.; Hoogenboom, R., Colorimetric Logic Gates Based on Poly(2-alkyl-2-oxazoline)-Coated Gold Nanoparticles. *Advanced Functional Materials* **2015**, *25* (17), 2511-2519.
24. Bloksma, M. M.; Weber, C.; Perevyazko, I. Y.; Kuse, A.; Baumgärtel, A.; Vollrath, A.; Hoogenboom, R.; Schubert, U. S., Poly(2-cyclopropyl-2-oxazoline): From Rate Acceleration by Cyclopropyl to Thermoresponsive Properties. *Macromolecules* **2011**, *44* (11), 4057-4064.
25. Irmukhametova, G. S.; Mun, G. A.; Khutoryanskiy, V. V., Thiolated Mucoadhesive and PEGylated Nonmucoadhesive Organosilica Nanoparticles from 3-Mercaptopropyltrimethoxysilane. *Langmuir* **2011**, *27* (15), 9551-9556.
26. Irmukhametova, G. S.; Fraser, B. J.; Keddie, J. L.; Mun, G. A.; Khutoryanskiy, V. V., Hydrogen-Bonding-Driven Self-Assembly of PEGylated Organosilica Nanoparticles with Poly(acrylic acid) in Aqueous Solutions and in Layer-by-Layer Deposition at Solid Surfaces. *Langmuir* **2012**, *28* (1), 299-306.
27. Fijten, M. W. M.; Haensch, C.; van Lankvelt, B. M.; Hoogenboom, R.; Schubert, U. S., Clickable Poly(2-Oxazoline)s as Versatile Building Blocks. *Macromolecular Chemistry and Physics* **2008**, *209* (18), 1887-1895.
28. Wiesbrock, F.; Hoogenboom, R.; Leenen, M. A. M.; Meier, M. A. R.; Schubert, U. S., Investigation of the Living Cationic Ring-Opening Polymerization of 2-Methyl-, 2-Ethyl-, 2-Nonyl-, and 2-Phenyl-2-oxazoline in a Single-Mode Microwave Reactor. *Macromolecules* **2005**, *38* (12), 5025-5034.
29. van der Pol, E.; Coumans, F. A. W.; Sturk, A.; Nieuwland, R.; van Leeuwen, T. G., Refractive Index Determination of Nanoparticles in Suspension Using Nanoparticle Tracking Analysis. *Nano Letters* **2014**, *14* (11), 6195-6201.
30. Bravo-Osuna, I.; Teutonico, D.; Arpicco, S.; Vauthier, C.; Ponchel, G., Characterization of chitosan thiolation and application to thiol quantification onto nanoparticle surface. *International Journal of Pharmaceutics* **2007**, *340* (1–2), 173-181.

31. Bressler, I.; Kohlbrecher, J.; Thunemann, A. F., SASfit: a tool for small-angle scattering data analysis using a library of analytical expressions. *J Appl Crystallogr* **2015**, *48*, 1587-1598.
32. Pedersen, J. S.; Gerstenberg, M. C., Scattering form factor of block copolymer micelles. *Macromolecules* **1996**, *29* (4), 1363-1365.
33. Smith, A. L., Infrared spectra-structure correlations for organosilicon compounds. *Spectrochimica Acta* **1960**, *16* (1), 87-105.
34. Evenhuis, C. J.; Guijt, R. M.; Macka, M.; Marriott, P. J.; Haddad, P. R., Variation of zeta-potential with temperature in fused-silica capillaries used for capillary electrophoresis. *Electrophoresis* **2006**, *27* (3), 672-676.
35. Ramachandran, R.; Somasundaran, P., Effect of Temperature on the Interfacial Properties of Silicates. *Colloid Surface* **1986**, *21*, 355-369.
36. Rodriguez, K.; Araujo, M., Temperature and pressure effects on zeta potential values of reservoir minerals. *J Colloid Interf Sci* **2006**, *300* (2), 788-794.
37. Perrin, D., The effect of temperature on pK values of organic bases. *Australian Journal of Chemistry* **1964**, *17* (4), 484-488.
38. Mori, T.; Maeda, M., Temperature-Responsive Formation of Colloidal Nanoparticles from Poly(N-isopropylacrylamide) Grafted with Single-Stranded DNA. *Langmuir* **2004**, *20* (2), 313-319.
39. Kujawa, P.; Winnik, F. M., Volumetric studies of aqueous polymer solutions using pressure perturbation calorimetry: A new look at the temperature-induced phase transition of poly(N-isopropylacrylamide) in water and D<sub>2</sub>O. *Macromolecules* **2001**, *34* (12), 4130-4135.
40. Mun, E. A.; Hannell, C.; Rogers, S. E.; Hole, P.; Williams, A. C.; Khutoryanskiy, V. V., On the Role of Specific Interactions in the Diffusion of Nanoparticles in Aqueous Polymer Solutions. *Langmuir* **2014**, *30* (1), 308-317.
41. Zhang, Z.; Maji, S.; da Fonseca Antunes, A. B.; De Rycke, R.; Hoogenboom, R.; De Geest, B. G., Salt-Driven Deposition of Thermoresponsive Polymer-Coated Metal Nanoparticles on Solid Substrates. *Angewandte Chemie International Edition* **2016**, *55* (25), 7086-7090.